

Dynamic Phase Transition Leading to Extraordinary Plastic Deformability of Thermoelectric SnSe₂ Single Crystal

Bangzhi Ge, Chao Li, Weiqun Lu, Haolin Ye, Ruoyan Li, Wenke He, Zhilei Wei, Zhongqi Shi, Dasol Kim, Chongjian Zhou,* Menghua Zhu,* Matthias Wuttig, and Yuan Yu*

Plastic/ductile inorganic van der Waals (vdW) thermoelectric semiconductors offer transformative advantages for high-performance flexible thermoelectric devices, which can displace the self-charge system of wearable electronics. However, the chemical origin of their plasticity remains unclear. Here, it is reported that the exceptionally large plastic strain of the bulk SnSe₂ crystal results from its polytype conversion under an external force. The SnSe₂ single crystal consists of a large-period polytype with 18R low-symmetry structure rather than the trigonal and hexagonal-phase that are frequently observed in the polycrystalline specimen. In situ applied pressure to the specimen drives a phase transition from low to high-symmetry, that is, from 18R to 4H, and finally to 2H-SnSe₂. First principle calculations corroborate that the dynamic phase transition is a pressure-activated process and only 15 MPa pressure erases their energy gaps, consistent with experimentally measured strain–stress curves. This dynamic phase transition results in superior and near isotropic plasticity along the direction parallel and perpendicular to the cleavage plane.

1. Introduction

Self-charging power supply bottlenecks the design of wireless wearable electronics.^[1] Thermoelectric semiconductors can directly convert the temperature gradient across materials into electricity through the Seebeck effect without mechanical noise and vibration.^[2] Accordingly, this technique shows broad potential to assemble self-powered, sustainable, and maintenance-free power sources to realize untethered wearable electronic devices by harvesting electricity from body heat.^[1] The efficiency of thermoelectric semiconductors is typically evaluated by the dimensionless figure of merit $ZT = S^2\sigma T/\kappa_{\text{tot}}$, where S is the Seebeck coefficient, σ is the electrical conductivity, T is the absolute temperature,

B. Ge, H. Ye, R. Li, C. Zhou, M. Zhu
State Key Laboratory of Solidification Processing
and Key Laboratory of Radiation Detection Materials and Devices
Ministry of Industry and Information Technology
Northwestern Polytechnical University
Xi'an 710072, China
E-mail: cjzhou@nwpu.edu.cn; mhzhu@nwpu.edu.cn

B. Ge, Z. Wei, Z. Shi
State Key Laboratory for Mechanical Behavior of Materials
Xi'an Jiaotong University
Xi'an 710049, China


C. Li
The Fifth Electronics Research Institute of Ministry of Industry and Information Technology
Guangzhou 510006, China

W. Lu
Institute of Advanced Semiconductors and Zhejiang Provincial Key
Laboratory of Power Semiconductor Materials and Devices
Hangzhou Innovation Center
Zhejiang University
Hangzhou 311200, China

W. He
Institute of Fundamental and Frontier Sciences
University of Electronic Science and Technology of China
610054 Chengdu, China

D. Kim, M. Wuttig, Y. Yu
Institute of Physics (IA)
RWTH Aachen University
52056 Aachen, Germany
E-mail: yu@physik.rwth-aachen.de

M. Wuttig
Peter Grünberg Institut (PGI 10)
Forschungszentrum Jülich
52425 Jülich, Germany

 The ORCID identification number(s) for the author(s) of this article can be found under <https://doi.org/10.1002/aenm.202300965>

© 2023 The Authors. Advanced Energy Materials published by Wiley-VCH GmbH. This is an open access article under the terms of the Creative Commons Attribution-NonCommercial License, which permits use, distribution and reproduction in any medium, provided the original work is properly cited and is not used for commercial purposes.

DOI: 10.1002/aenm.202300965

and κ_{tot} represents the total thermal conductivity, which contains contributions from electrons (κ_e) and phonons (κ_{lat}).^[13]

The ideal thermoelectric materials for wearable or flexible electronics must exhibit both high ZT values and exceptional plastic deformability.^[14] However, the majority of thermoelectric materials are brittle, and they usually fracture without any plastic deformation. This substantially limits their applications. The means of improving plasticity for thermoelectric materials has been limited to constructing inorganic/organic hybrid materials^[5] or discovering purely organic thermoelectric materials.^[6] The typical example of the former is an organic/inorganic hybrid superlattice of $\text{TiS}_2/[(\text{hexylammonium})_x(\text{H}_2\text{O})_y(\text{DMSO})_z]$, exhibiting a maximum ZT (ZT_{max}) of 0.28 at 373 K and an exceptionally high flexural modulus of ≈ 145 MPa at 300 K.^[7] However, this requires electrochemical intercalation and solvent exchange processes, and the material processing costs are very high.^[7] Pure organic thermoelectrics generally fail to deliver the high performance and air stability required for constructing efficient and durable thermoelectric devices.^[8] For example, the σ of thermoelectric molecular PEDOT:PSS was found to initially reach about 300 S m^{-1} , but rapidly air-degraded to nearly an insulator.^[9]

Among the state-of-the-art plastic thermoelectric systems, the most groundbreaking and promising one is the discovery of inorganic semiconductors that are plastic/ductile at room temperature,^[10] such as Ag_2S ^[11] and its alloys,^[12] and a class of binary two-dimensional van der Waals (2D vdW) chalcogenide crystals screened by high-throughput calculations.^[13] However, the extraordinarily large plasticity of 2D vdW materials has only been observable in single-crystals, and their polycrystalline cousins completely^[14] lose the plasticity and are as brittle as conventional thermoelectric materials. Despite the interlayer gliding and cross-layer dislocation slip in a deformed InSe crystal were observed by transmission electron microscopy (TEM),^[15] these results did not disclose the innate brittle nature of the polycrystalline sample. Understanding the origin of the plasticity of 2D vdW crystals can deepen our understanding of inorganic plastic semiconductors.

Herein, we have investigated the sample distortions under an applied force for a SnSe_2 single-crystal, which is a plastic/ductile bulk 2D vdW material with a promising thermoelectric performance of $ZT = 0.2$ at room temperature.^[16] The atomic-level structure of SnSe_2 reveals a large-period polytype with low-symmetry 18R rhombohedral structure, contradicting the previously reported 2H trigonal or 4H hexagonal structure. Upon in situ loading, we uncovered a dynamic phase transition from the low- to high-symmetry phase, namely, from the 18R phase converting into the high-symmetry 4H and 2H- SnSe_2 phases. We calculated the volume-dependent energy of each phase, revealing that 15 MPa pressure can erase the energy gap of those phases. The pressure also compacts SnSe_2 , localizing the electrons and reducing the plasticity. These findings confirm that the phase transition is a pressure-activated process. They also explain the poor plasticity of the polycrystal samples, which often show 4H and 2H structures due to the external pressure from sintering or grain boundaries leading to lower deformability. This work broadens our understanding of the deformation mechanism and provides a new design paradigm for flexible inorganic semiconductors.

2. Results and Discussion

Tin diselenide (SnSe_2) is a typical CdI_2 -type layer compound, in which the basic structural unit consists of two sheets of hexagonally close-packed selenium atoms with the tin atoms occupying the octahedral voids sandwiched between the selenium layers. However, reported results confirm that SnSe_2 possesses multiple polytypism, namely, it can form different crystal structures distinguished by variation of occupation sites along the c -axis. For example, we prepared a dense polycrystalline SnSe_2 pellet by solid-state reaction,^[14] which exhibits a zigzag structure with a 4H hexagonal P63mc space group throughout the specimen. In contrast, 2H trigonal P3m1 structure in addition to the dominant 4H phase was also observed in the compacted dense pellet.^[17] To understand the chemical origin and the presence of multiple phases, we pull a large single crystal of SnSe_2 with a diameter of 10 mm as displayed in **Figure 1a**. The crystal can be easily cleaved as indicated by the red arrow. It is interesting to note that the exfoliated thin layer exhibits exceptional plasticity and it can be folded and unfolded without any visible cracking (**Figure 1b,d**) and (**Figure S2**, Supporting Information), which is consistent with the previous report.^[16] **Figure 1e,f** presents stress-strain curves measured by compressing the rectangular specimens parallel and perpendicular to the cleavage plane, that is the c axis, respectively. Note that consistent results have been reached for measurements repeated at two independent synthesized crystals. The strain-stress data of InSe^[15] is also included for comparison. The results show that SnSe_2 did not fracture until the engineering strain arrives at 80% along both directions, and its plasticity is nearly isotropic. In contrast, InSe crystal exhibits anisotropic plasticity. This reflects that the plasticity mechanism of SnSe_2 may differ from InSe, whose deformability was attributed to mobile dislocations.^[15] On the other hand, we did not observe any plasticity in polycrystalline SnSe_2 composed of 4H or 2H SnSe_2 as shown in **Figure 1e,f**. These polycrystalline samples immediately fracture under compression $\approx 7\%$ of engineering strain.

Since the mechanical properties of given materials highly depend on their crystal structures and chemical bonds,^[18] we, therefore, considered the extraordinary plasticity of SnSe_2 arising from the crystal structure. X-ray diffraction (XRD) patterns of SnSe_2 single-crystal can be indexed to an 18R structure (**Figure S1**, Supporting Information), rather than the frequently observed 4H or 2H phase in the polycrystalline sample. This also supports our hypothesis that plasticity derives from polytype transitions.

Because XRD only probes structure at the microscale, we further investigated the microstructure of SnSe_2 at the atomic level using a spherical aberration-corrected scanning transmission electron microscope (Cs-STEM). The crystal was thinned down as a pillar along the direction perpendicular to the cleavage plane (**Figure 2a**), along which direction respective Sn and Se atoms are linearly aligned. As a consequence, this allows us to identify the stacking sequence of the SnSe_2 layer. **Figure 2b** displays a representative high-magnification STEM image, which reveals the entire matrix consisting of the triple atomic layers with no defects. To determine the atom arrangement of each layer, we collected an atomic resolution elemental map for the corresponding region using STEM-energy dispersive spectroscopy (EDS, **Figure 2c–f**). The smaller and fainter spheres throughout the matrix can be unambiguously assigned to Se, and the bigger and brighter spheres

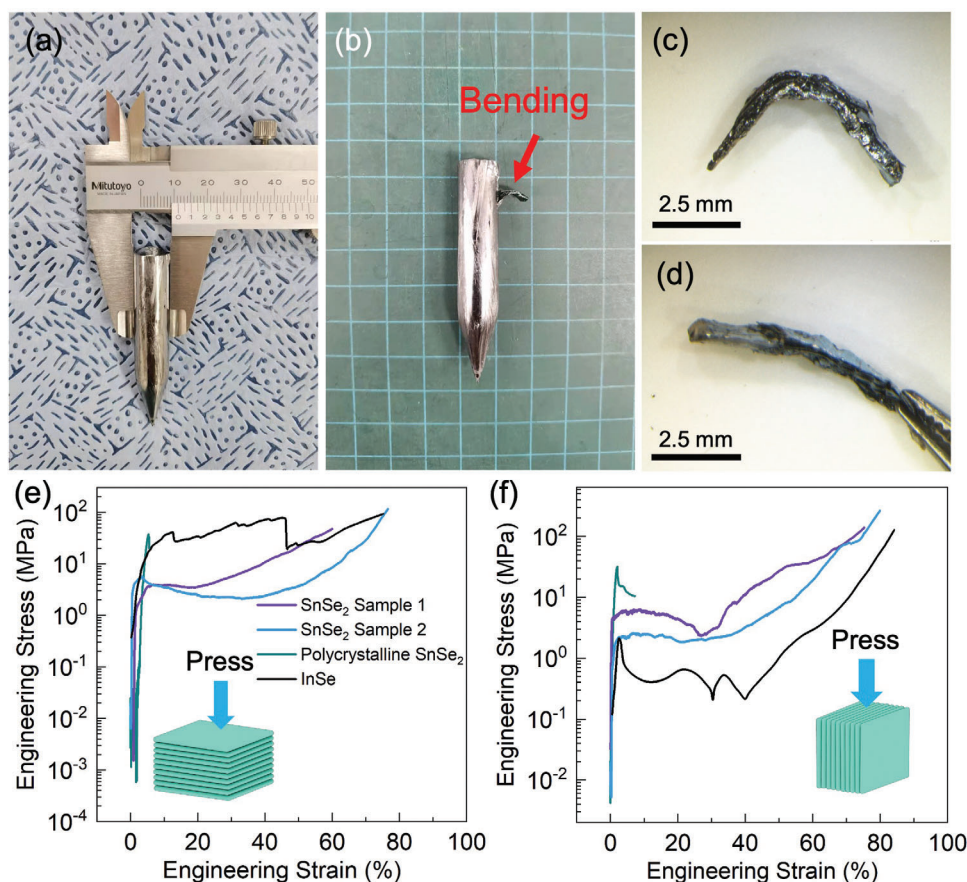


Figure 1. Mechanical properties of single crystal SnSe_2 a) SnSe_2 crystal with a diameter of ≈ 10 mm and length of ≈ 50 mm pulled by Bridgman method. b) A thin layer exfoliated from the bulk crystal exhibits extraordinary plasticity as indicated by the red arrow. c,d) The thin SnSe_2 crystal was folded and unfolded under optical microscopy, respectively, confirming the exceptional plasticity of the SnSe_2 crystal. Stress-strain curves of SnSe_2 single crystal and polycrystalline samples were collected by applying pressure e) perpendicular and f) parallel to the cleavage plane. The measurement was repeated for two independently synthesized crystals, showing consistent results. The data of $\text{InSe}^{[15]}$ are included for comparison.

interleaved between two adjacent Se atoms are Sn atoms. Accordingly, the specimen strictly follows the stoichiometric ratio of SnSe_2 without any secondary phase. The corresponding fast Fourier transform (FFT) image (Inset of Figure 2b) shows a single set of the diffraction pattern, corroborating its single-phase nature. The arrangement of the layer unit can be indexed as an 18R structure, in which nine individual SnSe_2 layers form the basic unit cell as outlined by the red rectangle (Figure 2b).

To resolve the structural distortion during deformation in real time, we applied force to the pillar-shaped specimen in situ, i.e., in the STEM chamber using a tungsten probe. Figure 2d images a pillar after compression. Even though the sample shows a discernible distortion, only a few dislocations are formed as indicated by the white arrow, corresponding to a dislocation density lower than $1.5 \times 10^7 \text{ cm}^{-2}$. This number density of dislocations is at least four orders of magnitude lower than conventional metallic materials^[19] and plastic InSe bulk crystal.^[15] Consequently, the macroscopic plasticity of SnSe_2 cannot be attributed to the movement and multiplication of dislocations. Figure 2e presents an atomic-resolution STEM image focusing on the region nearby the contact point (Figure S3, Supporting Information) between the tungsten probe and specimen. The undistorted and distorted

region forms a tightly joint phase boundary as indicated by the yellow dashed line. The former remains an 18R phase. In contrast, the pressure reconstructed the distorted region into multiple phases, in which 4H and 2H phases can be observed as indicated by the green and cyan dash boxes, respectively. Note that the distance between adjacent Se layers of the 18R structure is apparently wider than vdW gap reported for 4H and 2H structures, which implies that it can undergo deformation because of the larger space left for atoms to move under stress as discussed later. The atomic level EDS mapping reveals that the triple layer in the distorted region also consists of the Sn and Se atoms (Figure S4, Supporting Information), demonstrating that the phase change does not arise from an off-stoichiometry induced by an external force. As a result, the applied pressure drives the phase transition from 18R to 2H and 4H phases.

The in situ STEM experiment indicates that the crystal structure transition is associated with external pressure. Thus, we calculated the volume-dependent energy employing the first-principle calculations to study the structural evolution of SnSe_2 under pressure. The 18R, 4H, and 2H phases are constructed and relaxed to closely mimic the experimentally observed three crystal structures. To investigate the pressure-driven phase transitions,

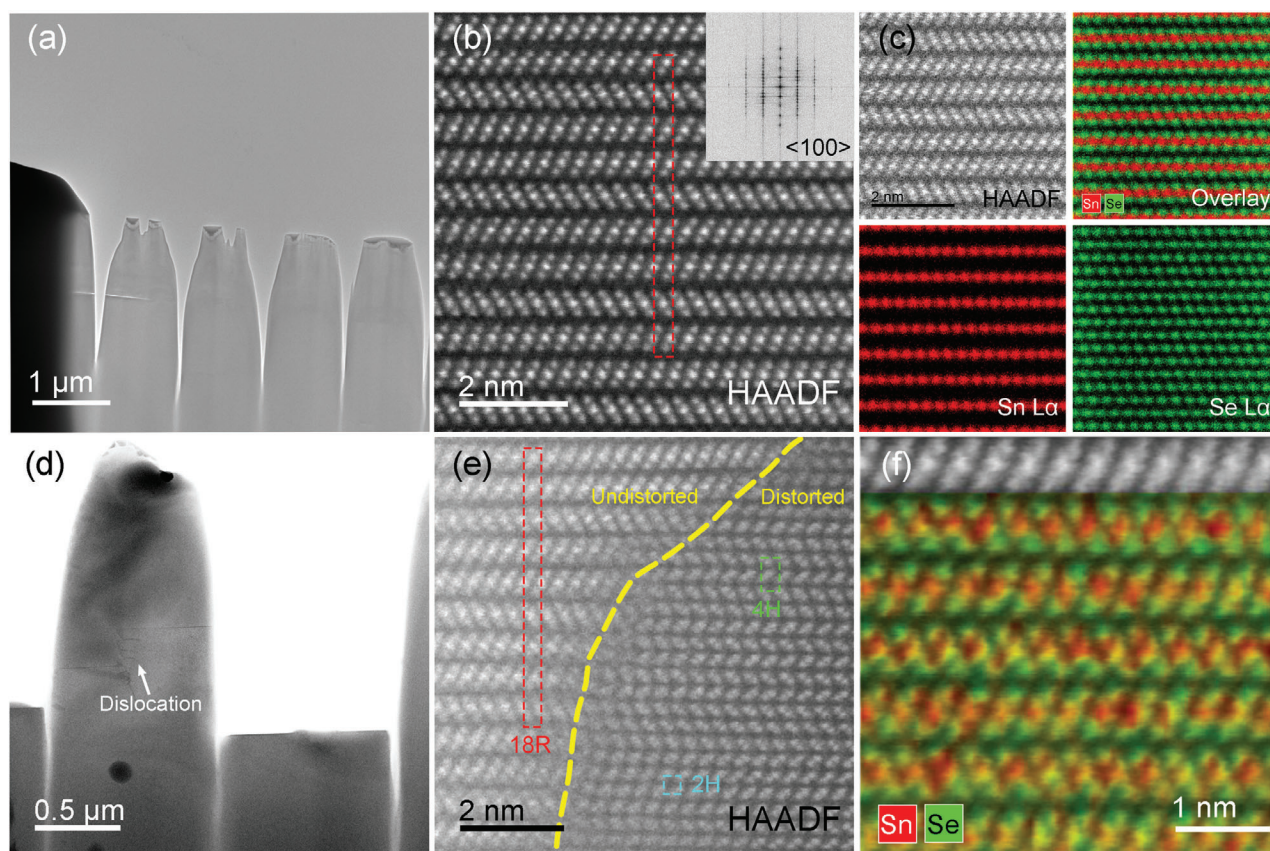


Figure 2. Structures and elemental distribution maps taken parallel to the $\langle 100 \rangle$ zone axis for the pillar-shaped specimens prepared from SnSe_2 crystal. a) Low-magnification transmission electron microscopy (TEM) image. b) Medium-magnification high-angle annular dark-field scanning transmission electron microscopy (HAADF-STEM) image showing the single 18R structure. Inset: electron diffraction pattern taken over the entire area presenting a single set of diffraction spots corresponding to 18R structure. c) Elemental distribution map by STEM energy dispersive spectroscopy (STEM-EDS). EDS signals directly recorded from Sn (red) and Se (green) are overlaid to show the distribution of the respective atoms. d) Low-magnification TEM image for resulting sample after in situ deformation. Dislocations embedded in the matrix are indicated by the white arrow. e) Medium-magnification HAADF-STEM image during the in situ deformation. The left part of the yellow broken line is undeformed showing the 18R structure. The right part is deformed showing the 4H structure mixing with a slight 2H structure. The unit cell of the 18R structure, 2H, and 4H structure is signified by the red, green, and blue dash lines, respectively. f) Elemental distribution map focusing on the 4H structure by STEM-EDS which is the overlaid image of the direct EDS signals from Sn (red) and Se (green).

we calculated the energy per atom with respect to the volume change of each phase of SnSe_2 and fitted them to the third-order Birch–Murnaghan equation of state (Figure 3a).^[20] 18R and 4H phase represent the metastable states, while 2H represents the stable state. Under compressive, differences in free energy between phases are reduced, indicating that compression facilitates the phase transition between 18R, 4H, and 2H phases, consistent with the experimental findings.

Note that the volume–energy curves of these structures intersect with each other at a volume change of $\approx 2\%$. Based on previously reported Young’s modulus of 78.77 GPa,^[16] this volume change corresponds to a pressure of 15 MPa. This is consistent with our previous report that only the 4H phase was observed in the spark plasma sintered (SPS) sample. It is because the SPS process usually involves pressure much larger than 15 MPa, and the phase transformation follows the lowest energy pathway once the pressure was released after sintering as denoted by the red arrow in Figure 3a,b. It should be noted that despite the 2H phase showing lower energy than the 4H

phase at no volume change, its energy gap is only 0.001 eV, which was rapidly removed upon volume shrink. In fact, the 4H phase shows energy lower than 2H at a pressure of ≈ 4 MPa. Accordingly, the 4H and 2H phases are competing phases after releasing the pressure. However, the 4H phase typically is the dominating phase in the polycrystalline sample because grain boundaries usually generate residual strain exceeding the threshold of ≈ 4 MPa, forcing the materials to remain in the 4H structure.^[21]

To connect the crystal structure with transport properties, we calculated the electronic band structures of these three phases in Figure 3c–e using DFT. All structures show nearly identical curvature and accordingly similar effective mass $m_0 = 0.5 m_e$ at the conduction band minima (CBM). As a result, the polytype structure conversion negligibly affects the thermoelectric performance. Indeed, the experimental thermoelectric performance of polycrystalline 4H SnSe_2 is comparable to that of 18R single crystal (Figure S5, Supporting Information), matching well with our calculations.

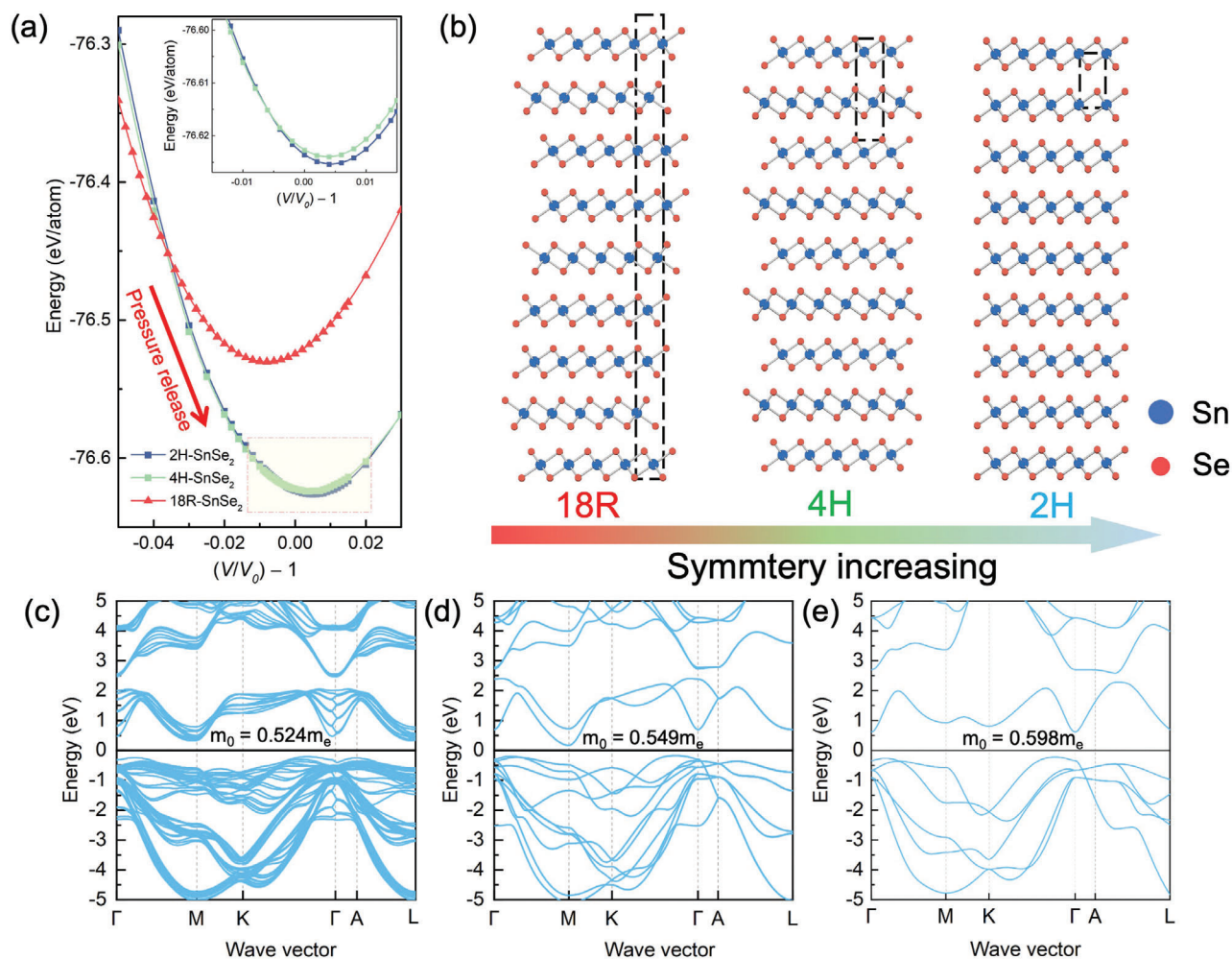


Figure 3. a) The energy with respect to the volume change of 2H, 4H, and 18R-SnSe₂ calculated by DFT. The positive and negative values represent lattice expansion and compression, respectively. b) Illustration of SnSe₂ structure transition upon applied pressure. The arrow indicates the structure consecutively changes from low symmetry 18R phase to the intermediate 4H phase, and finally to the high-symmetry 2H phase. Black dash boxes outline the unit cell of each structure. The electronic band structures of SnSe₂ for c) 18R, d) 4H, and e) 2H phases show nearly identical curvature and similar effective mass $m_0 = 0.5 m_e$ at the conduction band minima (CBM).

To further understand the relationship between phase transition and mechanical properties, we calculated the electron localization function (ELF). This measures the charge localization between adjacent atoms, directly appraising the chemical bonds between them. **Figure 4a–c** displays three-dimensional ELF for 18R, 4H, and 2H-SnSe₂, respectively. The color change from purple to red corresponds to electron transformation from full delocalization to perfect localization. According to the 3D-ELF contour map, the electrons surrounding Sn atoms are highly delocalized, indicating that the electrons behave as in metallic bonds. This finding is indeed consistent with our STEM images and relaxed supercell, which reveal a vdW gap of 3.13, 2.97, and 2.96 Å for 18R, 4H, and 2H-SnSe₂, respectively. These delocalized electrons can move freely within the matrix, facilitating the deformation of 18R-SnSe₂. The highly delocalized electrons shift the chemical bonds of 18R-SnSe toward metallic bonding, whereby the structure can undergo large deformation. In contrast, valence electrons are highly localized in 4H and 2H-SnSe₂. These results are consistent with our previous findings,^[14] which reveal an elec-

tron localization domain with a polar covalent interaction for the Sn–Se bond in 4H-SnSe₂. To quantify the change in the valence electron count upon the phase transitions, recently the predictive power of quantum-chemical bonding descriptors, i.e., the number of electrons shared (ES) and electrons transferred between adjacent atoms (TET)^[22] are calculated (Figures S6 and S7, Supporting Information). The interlayer interaction over vdW layers is considerably (13%) reduced when comparing the 18R phase with the 2H and 4H phases, consistent with the larger interlayer distances (6%). The valence electrons in the 18R phase, where the electronic cloud around the Se atom is relatively isolated, induce weak interlayer vdW forces, and hence an easier deformation. These results also help to understand why polycrystalline SnSe₂ does not show any plasticity: the localized electrons are constrained around the chemical bonds so that these structures are rigid and brittle.

We also calculated the mechanical properties to understand the impact of chemical bonds on them (see the Experiment Section for detail). Figure 4d–f presents the calculated Young's

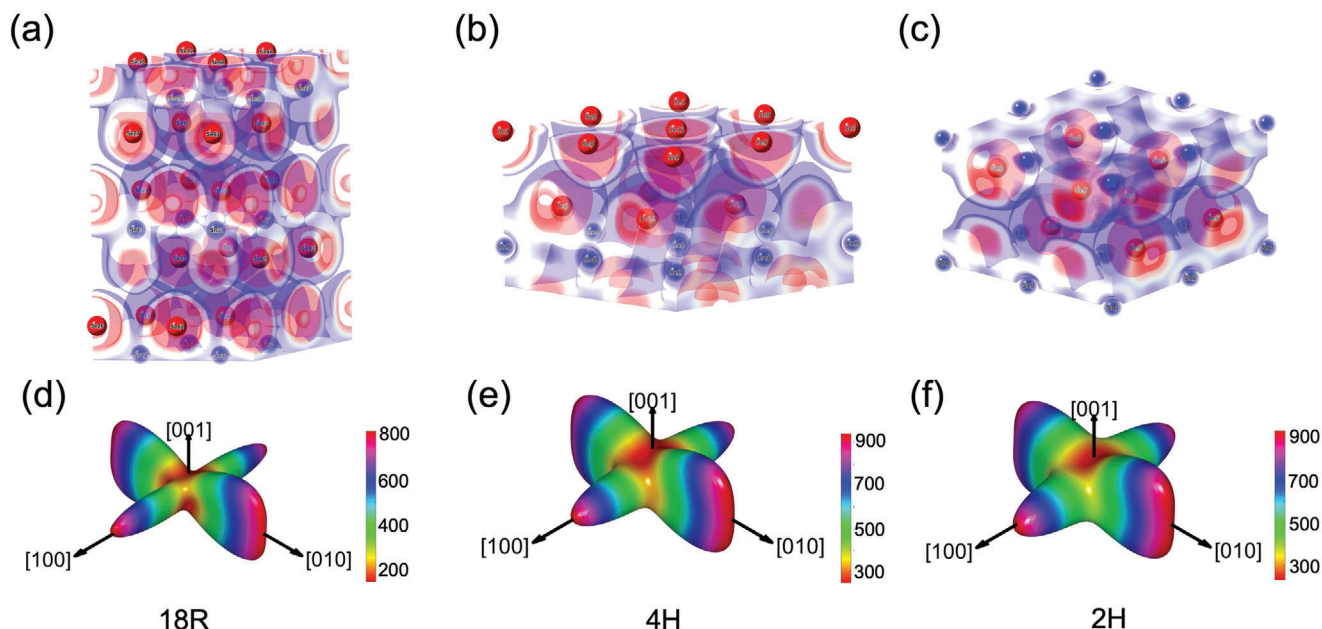


Figure 4. The electron localization function (ELF) and mechanical properties are extracted by first principle calculations. a–c) Three-dimensional ELF for 18R, 4H, and 2H-SnSe₂, respectively. The blue spheres represent Sn atoms, and the red spheres denote Se atoms. The color transition from purple to red corresponds to electron transformation from no localization to perfect localization. d–f) The calculated Young's modulus along three principal crystallographic directions for 18R, 4H, and 2H-SnSe₂, respectively.

modulus for 18R, 4H, and 2H-SnSe₂. The remaining mechanical properties, including shear modulus and Poisson ratio, are appended in the supporting information (Figures S8 and S10, Supporting Information). It is important to note that Young's modulus gradually increases as the phase consecutively converts from 18R to 4H, and finally to the 2H phase. It is because the delocalized electrons soften the chemical bonds, resulting in a lower Young's modulus. Additionally, the anisotropy of Young's modulus continuously decreases as symmetry increases. This matches well with our experimentally measured strain–stress curve, showing nearly isotropic performance even though the sample was deformed along two different directions.

3. Conclusion

Thermoelectric semiconductors tend to fail in a brittle manner because of their rigid chemical bonds. Searching for ductile thermoelectric materials is a highly sought-after goal. Recently, 2D vdW layered SnSe₂ single-crystal thermoelectric material is found to exhibit extraordinary plasticity and can be bent without forming visible cracks. Their plastic deformability was attributed to the long-range cation–anion Coulomb interaction mediated interlayer gliding and cross-layer dislocation slip. However, this mechanism does not explain the brittleness of polycrystalline SnSe₂. In this work, we precisely resolve the crystal structure of SnSe₂ statically and dynamically upon loading on the atomic level. The pristine SnSe₂ crystal consists of an 18R structure, which has never been observed in its polycrystalline cousins. In situ loading of pressure to the crystal leads to a low- to high-symmetry phase transition. By combining STEM experimental observations and first-principle calculations, the phase conversion pathway is determined to be from 18R to 4H, and finally

to the 2H phase upon compression. These results disclose a new mechanism underneath the exceptional plasticity of SnSe₂, extending our understanding of plasticity and the design of flexible inorganic semiconductors.

4. Experimental Section

Synthesis and Single Crystal Growth: Reagents of Sn and Se (99.999%, American Elements) were used as received. Ingots (≈20 g) with the nominal compositions SnSe₂ were synthesized by reacting an appropriate molar ratio of starting reagents in an evacuated fused silica tube (≈10^{−5} Torr) at 973 K for 6 h, followed by quenching to ice water. The obtained ingots were subsequently annealed at 773 K for 72 h and naturally cooled to room temperature. The products were hand-ground by an agate mortar and pestle to a fine powder in an Ar-filled glove box. The resulting powder was loaded into an evacuated cone-shaped quartz tube and placed in a vertical Bridgman furnace. The crystal was grown at a temperature of 973 K with a speed of 1 mm h^{−1}. These preparation processes were important for obtaining a high-quality single crystal with uniform element distribution. The polycrystalline SnSe₂ was prepared by melting synthesis combined with SPS. The above ingot was hand-ground by an agate mortar and pestle to fine powders in an Ar-filled glove box. The resulting powders were consolidated at 773 K for 5 min under an axial pressure of 50 MPa in a vacuum using SPS (SPS-211Lx, Fuji Electronic Industrial Co., Japan).

X-Ray Diffraction (XRD): XRD patterns were collected using Cu Kα (λ = 1.5418 Å) graphite monochromatized radiation on a SmartLab Rigaku powder X-ray diffractometer operating at 40 kV and 20 mA.

Scanning Transmission Electron Microscopy (STEM): For STEM, the specimen was thinned down as a pillar in the direction perpendicular to the cleavage plane, namely, along the <100> zone axis by focused ion beams (FIB, Helios 650, FEG, FEI) with a dual beam microscope employing gallium ion milling.^[23] Before the ion milling, a thin layer of carbon was sputtered to the surface of the specimen for protecting the sample. Structures and chemical compositions were analyzed by a spherical aberration-

corrected JEM ARM-200F microscope (Cold FEG Type, JEOL) equipped with an SDD type EDS detector (Solid Angle 0.9-sr, X-MaxN 100TLE, OXFORD) at 200 kV. In high-angle annular dark-field STEM (HAADF-STEM) images, the point-to-point resolution was about 80 pm after the spherical aberration correction and the angular range of the annular detector employed was from 68 to 280 rad. All STEM images were obtained by a high-resolution CCD detector with a $2k \times 2k$ pixel device in the GIF-QuantumER imaging filter (GATAN). For STEM-EDS investigation, chemical maps were recorded with a probe size of 0.13 nm and a probe current of 40 pA.

First Principle Calculations: We performed the first-principles calculation utilizing the Perdew–Burke–Ernzerhof (PBE)^[24] implemented in the Vienna ab initio simulation package (VASP) code.^[25] To describe vdW interactions, the strongly constrained and appropriately normed meta-GGA functional with the revised Vydrov–van Voorhis nonlocal correlation functional (SCAN+rVV10) was employed.^[26] Meta-GGAs offer higher accuracy compared to GGAs, but their computational cost is significantly higher. To investigate the pressure-induced phase transition of SnSe₂, Vesta was used^[27] to construct three different crystal structures, including 2H, 4H, and 18R-SnSe₂. In the calculations, the energy at 400 eV was truncated. All the atoms were optimized for geometric structure until the variation of the total energy was below 1×10^{-6} eV, the relaxation would not stop until all forces were less than 1×10^{-2} eV Å⁻¹. Furthermore, the Brillouin zone (BZ) was sampled with $9 \times 9 \times 4$, $9 \times 9 \times 2$, and $9 \times 9 \times 1$ k-point mesh generated by the Γ -centered for the 2H, 4H, and 18R-SnSe₂ phases, respectively. Finally, postprocessing software was employed to extract the mechanical properties of each phase.

Supporting Information

Supporting Information is available from the Wiley Online Library or from the author.

Acknowledgements

C.Z. acknowledges the financial support from Fundamental Research Funds for the Central University (D5000220051). M.Z. acknowledges the financial support from the National Natural Science Foundations of China (Nos. 62104194) and the Research Fund of the State Key Laboratory of Solidification Processing (NPU), China (No.2022-TS-07). All authors from RWTH acknowledge the support of DFG (German Science Foundation) within the SFB 917 (Nanoswitches). C.L. acknowledges the support from the Independent Research Foundation of Guangxi Key Laboratory of Information Materials (Grant No.211017-K).

Open access funding enabled and organized by Projekt DEAL.

Conflict of Interest

The authors declare no conflict of interest.

Author Contributions

B.G., C.L., and W.L. contributed equally to this work. C.Z., Y.Y., and M.W. conceived the project. C.Z., B.G., W.L., H.Y., R.L., and M.Z. prepared the samples and measured their mechanical properties. C.L. carried out the STEM experiments. B.G. performed the first principle calculations. C.Z. and Y.Y. constructed the structure, prepared the figures, and wrote the draft. All authors edited the manuscript and approved the submission of this work.

Data Availability Statement

The data that support the findings of this study are available from the corresponding author upon reasonable request.

Keywords

inorganic semiconductors, phase transition, plasticity, thermoelectric, van der Waals chalcogenides

Received: March 30, 2023

Revised: May 4, 2023

Published online: May 26, 2023

- [1] R. Liu, Z. L. Wang, K. Fukuda, T. Someya, *Nat. Rev. Mater.* **2022**, *7*, 870.
- [2] a) Y. Ding, Y. Qiu, K. Cai, Q. Yao, S. Chen, L. Chen, J. He, *Nat. Commun.* **2019**, *10*, 841; b) X. Lou, S. Li, X. Chen, Q. Zhang, H. Deng, J. Zhang, D. Li, X. Zhang, Y. Zhang, H. Zeng, *ACS Nano* **2021**, *15*, 8204; c) W. He, D. Wang, H. Wu, Y. Xiao, Y. Zhang, D. He, Y. Feng, Y.-J. Hao, J.-F. Dong, R. Chetty, L. Hao, D. Chen, J. Qin, Q. Yang, X. Li, J.-M. Song, Y. Zhu, W. Xu, C. Niu, X. Li, G. Wang, C. Liu, M. Ohta, S. J. Pennycook, J. He, J.-F. Li, L.-D. Zhao, *Science* **2019**, *365*, 1418.
- [3] a) Y. Zhou, L. D. Zhao, *Adv. Mater.* **2017**, *29*, 1702676; b) P. Ying, X. Li, Y. Wang, J. Yang, C. Fu, W. Zhang, X. Zhao, T. Zhu, *Adv. Funct. Mater.* **2017**, *27*, 1604145.
- [4] a) Q. Meng, Y. Qiu, K. Cai, Y. Ding, M. Wang, H. Pu, Q. Yao, L. Chen, J. He, *ACS Appl. Mater. Interfaces* **2019**, *11*, 33254; b) Y. Wang, L. Yang, X. L. Shi, X. Shi, L. Chen, M. S. Dargusch, J. Zou, Z. G. Chen, *Adv. Mater.* **2019**, *31*, 1807916.
- [5] a) W. Ren, Y. Sun, D. Zhao, A. Aili, S. Zhang, C. Shi, J. Zhang, H. Geng, J. Zhang, L. Zhang, *Sci. Adv.* **2021**, *7*, eabe0586; b) E. W. Zaia, A. Sahu, P. Zhou, M. P. Gordon, J. D. Forster, S. Aloni, Y.-S. Liu, J. Guo, J. J. Urban, *Nano Lett.* **2016**, *16*, 3352.
- [6] O. Bubnova, Z. U. Khan, A. Malti, S. Braun, M. Fahlman, M. Berggren, X. Crispin, *Nat. Mater.* **2011**, *10*, 429.
- [7] C. Wan, X. Gu, F. Dang, T. Itoh, Y. Wang, H. Sasaki, M. Kondo, K. Koga, K. Yabuki, G. J. Snyder, *Nat. Mater.* **2015**, *14*, 622.
- [8] a) B. Russ, A. Glauddell, J. J. Urban, M. L. Chabiny, R. A. Segalman, *Nat. Rev. Mater.* **2016**, *1*, 16050; b) T. Sun, L. Wang, W. Jiang, *Mater. Today* **2022**, *57*, 121.
- [9] D. J. Yun, J. Jung, Y. M. Sung, H. Ra, J. M. Kim, J. Chung, S. Y. Kim, Y. S. Kim, S. Heo, K. H. Kim, *Adv. Electron. Mater.* **2020**, *6*, 2000620.
- [10] H. Chen, T. R. Wei, K. Zhao, P. Qiu, L. Chen, J. He, X. Shi, *InfoMat* **2021**, *3*, 22.
- [11] X. Shi, H. Chen, F. Hao, R. Liu, T. Wang, P. Qiu, U. Burkhardt, Y. Grin, L. Chen, *Nat. Mater.* **2018**, *17*, 421.
- [12] a) S. He, Y. Li, L. Liu, Y. Jiang, J. Feng, W. Zhu, J. Zhang, Z. Dong, Y. Deng, J. Luo, *Sci. Adv.* **2020**, *6*, eaaz8423; b) Y. Fu, S. Kang, H. Gu, L. Tan, C. Gao, Z. Fang, S. Dai, C. Lin, *Adv. Sci.* **2023**, *10*, 2207642; c) Y. Wang, A. Li, H. Hu, C. Fu, T. Zhu, *Adv. Funct. Mater.* **2023**, *2300189*.
- [13] Z. Gao, T.-R. Wei, T. Deng, P. Qiu, W. Xu, Y. Wang, L. Chen, X. Shi, *Nat. Commun.* **2022**, *13*, 7491.
- [14] C. Zhou, Y. Yu, X. Zhang, Y. Cheng, J. Xu, Y. K. Lee, B. Yoo, O. Cojocaru-Mirédin, G. Liu, S.-P. Cho, M. Wuttig, T. Hyeon, I. Chung, *Adv. Funct. Mater.* **2019**, *30*, 1908405.
- [15] T.-R. Wei, M. Jin, Y. Wang, H. Chen, Z. Gao, K. Zhao, P. Qiu, Z. Shan, J. Jiang, R. Li, *Science* **2020**, *369*, 542.
- [16] T. Deng, Z. Gao, P. Qiu, T. R. Wei, J. Xiao, G. Wang, L. Chen, X. Shi, *Adv. Sci.* **2022**, *9*, 2203436.
- [17] C. Liu, Z. Huang, D. Wang, X. Wang, L. Miao, X. Wang, S. Wu, N. Toyama, T. Asaka, J. Chen, E. Nishibori, L.-D. Zhao, *J. Mater. Chem. A* **2019**, *7*, 9761.
- [18] a) G. Li, U. Aydemir, S. I. Morozov, M. Wood, Q. An, P. Zhai, Q. Zhang, W. A. Goddard, G. J. Snyder, *Phys. Rev. Lett.* **2017**, *119*, 215503; b) Q. Liang, D. Yang, F. Xia, H. Bai, H. Peng, R. Yu, Y. Yan, D. He, S.

- Cao, G. Van Tendeloo, G. Li, Q. Zhang, X. Tang, J. Wu, *Adv. Funct. Mater.* **2021**, 31, 2106938.
- [19] J. Zhang, C. Somsen, T. Simon, X. Ding, S. Hou, S. Ren, X. Ren, G. Eggeler, K. Otsuka, J. Sun, *Acta Mater.* **2012**, 60, 1999.
- [20] Y. Zhang, Y. Guo, Z. Liao, C. Liu, P. Huai, Z. Zhu, X. Ke, *High Pressure Res.* **2020**, 40, 267.
- [21] J. He, S. N. Girard, M. G. Kanatzidis, V. P. Dravid, *Adv. Funct. Mater.* **2010**, 20, 764.
- [22] J.-Y. Raty, M. Schumacher, P. Golub, V. L. Deringer, C. Gatti, M. Wuttig, *Adv. Mater.* **2018**, 31, 1806280.
- [23] C. Zhou, Y. Yu, Y.-L. Lee, B. Ge, W. Lu, O. Cojocaru-Mirédin, J. Im, S.-P. Cho, M. Wuttig, Z. Shi, I. Chung, *J. Am. Chem. Soc.* **2020**, 142, 15172.
- [24] J. P. Perdew, K. Burke, M. Ernzerhof, *Phys. Rev. Lett.* **1996**, 77, 3865.
- [25] a) A. Savin, O. Jepsen, J. Flad, O. K. Andersen, H. Preuss, H. G. von Schnering, *Angew. Chem., Int. Ed. Engl.* **1992**, 31, 187; b) G. Kresse, J. Furthmüller, *Phys. Rev. B* **1996**, 54, 11169.
- [26] a) H. Peng, Z.-H. Yang, J. P. Perdew, J. Sun, *Phys. Rev. X* **2016**, 6, 041005; b) J. Sun, A. Ruzsinszky, J. P. Perdew, *Phys. Rev. Lett.* **2015**, 115, 036402.
- [27] K. Momma, F. Izumi, *J. Appl. Crystallogr.* **2011**, 44, 1272.